PCCP

Accepted Manuscript

ROYAL SOCIETY OF CHEMISTRY

www.rsc.org/pccp

A facile route for the synthesis of nanostructured oxides and hydroxides of cobalt using laser ablation synthesis in solution (LASIS)

Sheng Hu[2,4], Chad Melton[3], Dibyendu Mukherjee[1,2,4*]

[1]Department of Mechanical, Aerospace, and Biomedical Engineering; [2]Department of Chemical and Biomolecular Engineering; [3]Department of Physics and Astronomy; [4]Sustainable Energy Education and Research Center (SEERC); University of Tennessee, Knoxville, Tennessee, 37996

Abstract

We used pulsed laser ablation synthesis in solution (LASIS) to produce cobalt oxide/hydroxide nanoparticles (NPs) with tailored size, morphology and structure at different laser fluences, wavelengths (532 and 1064 nm) and solvent conditions. Specifically, LASIS on bulk Co in the presence and absence of O_2 in aqueous solution initially produces cobalt monoxide (CoO) and single crystal β-cobalt hydroxide (β-$Co(OH)_2$) nanoparticles (NPs) respectively, that finally transform into cobaltosic oxide (Co_3O_4) through oxidation and/or thermal decomposition. Transmission electron microscopy (TEM) and scanning mobility particle sizer (SMPS) measurements on the final products reveal bimodal size distributions of agglomerated NPs (for 1064 and 532 nm laser) at low laser fluences, where the ablation mechanism is dominated by vaporization and normal boiling. In contrast, the more efficient and predominant explosive boiling at higher laser fluences produces mono-modal size distributions of spherical shaped primary NPs in agglomerates. Furthermore, higher absorbance of 532 nm laser by solution-phase colloidal NPs re-ablates them into spherical shapes of larger sizes (~13-22 nm) as compared to the ones from 1064 nm LASIS (~10-14 nm), while rendering 532 nm LASIS less productive than 1064 nm LASIS over extended time. Finally, Co_3O_4 nanorods with enhanced localized surface plasmon resonance (LSPR) are synthesized at high pH (pH≥13) and low laser fluence (<5 mJ/cm^2) conditions. Such nanostructured materials are promising candidates as photocatalysts or additives in nanocomposite materials with enhanced light absorption properties.

Introduction:

In recent years, laser ablation synthesis in solution (LASIS) has attracted tremendous research interests[1–5] among the diverse nanoparticle (NP) synthesis routes. The specific interest in LASIS arises due to its distinctive advantages of being a simple, elegant and yet chemical-free technique that requires minimal manual operation and low start-up cost.[2,6–10] In the past, LASIS has been used to synthesize various types of NPs comprising of heavy metals,[5,8] transition metals,[3,11]

inter-metallic nano-colloids.[12,13] Additionally, a few morphologically complex nanostructures such as core-shell,[14,15] and hollow[16] NPs have also been synthesized using LASIS. Such synthesis routes become critical for the production of metal/intermetallic NPs with controlled size, shape, structure, and surface chemistry that finds wide applications in catalytic fields.[3,17–19] Although highly suited for its ability to produce controlled nanostructures in the absence of any external chemical reagents and/or, surfactants/ligands, LASIS bears the disadvantages of relatively low productivity and poor control on shape/size.[2,10]

Added to this, the complex physics of laser-matter interactions involved during the nucleation of NPs via LASIS is still not clearly understood.[10,20] Unlike the relatively straight forward NP formation mechanism during laser ablation in gas phase,[21] the pulsed laser beam during LASIS creates a confined plasma plume with extremely high temperature and pressure on the metal target surface that results in thermal vaporization of the metal target (explosive boiling).[20] Previous works have reported that the seeding NPs start to form inside an oscillating cavitation bubble resulting from the expanding plasma plume as well as undergo collisional quenching at the bubble-liquid interface when the bubbles collapse.[22] Overall, the entire LASIS process can be divided into six stages within the first few milliseconds of the onset of ablation, i.e., laser pulse penetration in the liquid, absorption of laser pulse by target, ablated material detachment from target, plasma plume evolution and quenching, expansion and collapse of cavitation bubble, NP growth and aggregation.[2] Among all these stages, the detachment of ablated material plays a critical role in initiating the nucleation process, which is dominated by mainly three types of ablation mechanisms, vaporization, normal boiling and explosive boiling.[20] The onset of these mechanisms are controlled by the target surface temperature, which is dictated by laser fluence (laser energy per unit area) and pulse duration time. Specifically, vaporization refers to the emission of particles by sublimation or evaporation due to electron-phonon coupling, and theoretically, can occur at any laser fluence. Normal boiling, with low laser energy requirement usually induces heterogeneous nucleation and is strongly affected by the bubble diffusion. Finally, explosive boiling initiates the most efficient

ablation mechanism at superheating conditions that results in homogeneous nucleation at a much higher energy threshold value than normal boiling.[2,20]

The structures, shapes and properties of NPs synthesized by LASIS are dictated by the laser parameters and environmental conditions of the experiment. The former includes laser fluence,[5,20] wavelength,[23] pulse duration time,[24] repetition rate, spot area, etc. Both laser fluence and pulse duration time play the crucial role in determining how much heat can be absorbed by the target during the ablation process, thereby controlling the target surface temperature and the corresponding ablation mechanism.[5] The choice of laser wavelength mainly affects the laser energy penetration through the liquid column and the re-absorption by solution-phase colloidal NPs.[23] This, in turn, controls the extent of "re-ablation" of the already-formed NPs in solution, thereby modifying the final sizes and shapes of synthesized NPs. In this regard, shorter laser wavelengths usually bear larger impact on the re-structuring of solution phase NPs due to higher absorption by the particles.[20] On the other hand, the environmental parameters such as solution-phase oxygen content and pH value also influence the composition as well as the shape and size of the synthesized NPs by controlling the solution-phase ion concentration that dictates the nanocrystal growth directions.[25,26] To this end, previous studies by P. Blandin et al. indicated the ability to control size and surface oxidation of crystalline Si-based NPs by tuning the amount of dissolved oxygen in water during LASIS.[27] On a similar note, previous work by S. C. Singh et al. have also shown that injecting solution phase oxygen during LASIS on Zn reduced the particle size and $Zn(OH)_2$/ZnO ratio but increased the crystallinity of products.[28]

Specifically, cobalt oxide (CoO_x) NPs in two oxidation states, namely cobalt (II) monoxide (CoO) and cobaltosic (II,III) oxide (Co_3O_4), have attracted significant interest in the research community as one of the most promising earth-abundant transition metal oxides with catalytic activities towards water oxidation (photocatalysis), carbon monoxide (CO) oxidation, toluene oxidation, hydrogen evolution, etc.[3,19,29–33] Our specific interest in CoO_x NPs stems from their application as photocatalysts for solar water-splitting in an effort to mimic the photosynthetic

systems.[3,19,34,35] On the other hand, β-cobalt hydroxide (β-$Co(OH)_2$), an intermediate en route to Co_3O_4 formation, has high energy density and bears great potential for its use as electronic capacitors and electrode materials in Li-Ion batteries.[36–38] Previous studies have reported chemical routes for the synthesis of CoO_x NPs[29,32,39–42] and β-$Co(OH)_2$ nanocrystals[43,44] of various sizes and shapes. However, such synthesis routes inevitably leave unwanted chemicals including surfactants, leftover reducing agents and different kinds of by-products on the catalyst surface that dramatically retard their performances.[45,46] In recent years, laser ablation techniques have been successfully utilized to synthesize Co_3O_4 NPs that indicate higher catalytic activities for water oxidation, as compared to the ones synthesized via wet chemical techniques.[3] Such enhancement in catalytic activities is mainly attributed to the green synthesis route of LASIS that prevents any surface contamination from excess chemicals. However, few studies have explored in details the role of experimental and laser parameters in fine-tuning the laser ablation mechanism to enable systematic tailoring of the shape, structure and chemical composition of CoO_x/β-$Co(OH)_2$ NPs synthesized via LASIS.

The present study uses an in-house designed LASIS setup to investigate the capabilities of LASIS to synthesize CoO_x/β-$Co(OH)_2$ nanostructures with tailored size, morphology and composition by tuning various solution-phase experimental as well as laser parameters. Specifically, the role of laser wavelengths (1064 and 532 nm), laser fluences, aging time, ablation time, oxygen content and pH conditions in solution are systematically studied to provide a detailed mechanistic picture behind the controlled synthesis of various nanostructures using LASIS.

Experimental:

A. LASIS setup

The in-house built LASIS setup, as shown by the schematic in Fig. 1, houses a Q-switched Nd:YAG pulsed laser (Manufacturer: Brilliant Inc.; Model: Brilliant Easy) equipped with 1st and 2nd harmonic generators that provide 532 nm and 1064 nm

wavelengths of 165 and 330 mJ/full pulse energy, respectively at 10 Hz repetition rate and 4 ns pulse duration. The laser beam is focused at the surface of a metal target immersed in a desired liquid medium inside a sealed stainless steel reactor cell. In the current design, the laser beam is focused with a convex lens (focal length: 75 mm), and the focused beam passes through a high damage threshold tested laser window on the cell. The cell is provided with four side-viewing windows to accurately view and adjust the laser focal point. A gas inlet and outlet on the cell allows for suitable purging with inert gases. The metal target platform, mounted on a stepper motor, rotates continuously to enable uniform ablation from the surface. The reactor cell is also provided with heating rods along with a thermocouple for accurate monitoring of solution temperature and a sonic dismembrator for in situ de-agglomeration of the synthesized NPs. Additionally, a programmable injection unit is attached to the cell that allows for simultaneous introduction of metal salt precursor solutions for chemical reduction methods.

B. LASIS on Co

The Co pellets bought from Kurt J. Lesker (99.95% purity, 1/4" diameter×1/4" height) were used as targets, which were covered by 35 ml of de-ionized water (DI-water; Purity = 99.9%; Conductivity = 18.2 MΩ/cm at 25°C) during laser ablation. The distance between the target and water surface was measured to be 5 cm, and the corrected focal length was estimated to be 85 mm upon taking into account the refraction through water. Based on these measurements, the lens to surface distance (LTSD) was accurately determined for both laser wavelengths. For comparison of Co NPs generated via LASIS at different laser fluences, all samples were ablated for 15 min at room temperature. All experiments were conducted with simultaneous ultrasonication. The Co target was rotated by the stepper motor at a speed of 0.3 rpm during ablation. The aging test was conducted in standard ambient temperature and pressure, i.e., 298.15 K and 101 kPa. For O_2 free LASIS, N_2 was purged in water for 30 min before experiments and purged above water surface during experiments. The oxygen concentration in solution measured before and after ablation process is 0.32

mg/L and 0.35 mg/L respectively as compared to the corresponding value of ~5 mg/L for dissolved O_2 at atmospheric pressure in unpurged solution. The small increase of O_2 concentration is attributed to the minor contamination during the measurement using the oxygen meter. The resulting oxygen to NP weight ratio is calculated to be around 1:100. For re-ablation experiments, NP colloids were transferred to a 30 ml vial, and subsequently, ablated with the laser beam being focused at the center of the solution. For NP productivity tests, ablation was carried out for different periods of time using the unfocused laser beam (0.3 J/cm^2 for both 1064 nm and 532 nm laser). For different pH studies, HCl (Cole-Parmer, 36.5-38%) and KOH (Fisher Scientific, ＞85%) were used as the acid and base reagents for the desired acidic and alkaline conditions. The obtained colloidal solution was centrifuged at 5000 rpm for 15 min and then washed/decanted with DI-water for two times.

C. Characterization

A Zeiss Libra 200MC monochromated transmission electron microscope (TEM) was used with an accelerating voltage of 200 kV for regular TEM, selected area diffraction (SAED) and high resolution image (HRTEM) analysis.

The NP size distributions in aerosol form were collected via scanning mobility particle sizer^{TM} (SMPS^{TM}) spectrometer made by TSI Inc. (Model: 3936). The aerosolized NPs were generated using an atomizer operating at 30 psi (g) gas pressure. The sample flow rate and sheath flow rate were set to be 1.5 lpm and 15 lpm respectively. The accuracy of SMPS is reported to be 0.05 nm.

Raman spectra were measured via a Renishaw M1000 micro-Raman spectrometer with 532 nm, 900 μw laser excitation and 120 s acquiring time. Samples for Raman spectra were made by drop casting NP solution on an aluminum foil. The measured Raman shifts were calibrated against a cyclohexane standard.

Inductively coupled plasma optical emission spectroscopy (ICP-OES) (Perkin Elmer, Optima 4300 DV) was used to measure the concentration of NPs. Standard cobalt dichloride solution (≥99%) was used for calibration. UV-Vis absorption measurement (Biotek, Synergy H1) was scanned over the wavelength range of 300nm

to 900nm at a scan rate of 2 nm/step.

Results and discussion:

A. Chemical pathway for the products during LASIS on Co

The products from LASIS (532 nm laser) on Co with different aging time and dissolved oxygen amount were first investigated. TEM images and corresponding selected area electron diffraction (SAED) patterns for fresh and aged NPs produced via LASIS on cobalt (shown in Fig. 2) indicate large networks of heavily coalesced nanostructures for freshly synthesized products, as seen from Fig. 2 (a). Corresponding SAED pattern in Fig. 2 (c) exhibits four diffraction rings with diameters of 8.1, 9.39, 13.3, and 15.4 (1/nm) that agrees well with the (111), (200), (220) and (311) lattice planes of cobalt monoxide (CoO) (JCPDS #43-1004), as indicated in Table 1 comparing the transformed d-spacings with the respective standard values. However, after three days of ageing, the aforementioned nanostructures transform into dendritic agglomerates of spherical NPs (Fig. 2 (b)). The respective SAED patterns indicate the diffraction rings for CoO to evolve into those for cobaltosic oxide (Co_3O_4) (JCPDS #43-1003), as demonstrated in Fig. 2 (d) and Table 1. The above phenomena indicate that LASIS on Co initially produces CoO that, over a period of time, further oxidizes to Co_3O_4 in the colloidal solution. These results reveal the chemical pathway for the formation of Co_3O_4 via intermediate oxidization states during LASIS, as expected under extreme temperature conditions (>1000 ^oC) and is contrary to the commonly reported Co_3O_4 as the direct product of LASIS on Co.[3] The findings are further confirmed by the respective d-spacings from HRTEM images in Figs. 3 (a) & (b) as well as Raman spectra in Figs. 3 (c) & (d), where the two main peaks for Raman shifts at ~693 cm^{-1} and ~484 cm^{-1} correspond to the Raman active modes (E_g and A_{1g}) for Co(II, III)O_x. Specifically, the peak at ~523 cm^{-1} is assigned to Raman active mode of A_{2g}, a distinctive peak for Co_3O_4,[47] as also supported by standard Raman spectra for CoO and Co_3O_4 (Fig. S3 in supplementary information). The obvious A_{2g} peak at 524 cm^{-1} in Fig. 3 (d) indicates the strong

presence of Co_3O_4 in the sample aged for three days as compared to a weak presence of the peak in Fig. 3 (c). The two small peaks for typical Co_3O_4 sample missing at 197 nm and 624 nm for the aged sample in Fig. 3 (d) is possibly due to the low sample deposition amount. Bearing in mind that the standard Raman spectra is for bulk Co_3O_4 samples, the signal intensities for the 197 nm and 624 nm spectral lines most probably have been too small to be detected above the background noise in the spectral profile. For all those characterizations, the presence of a small portion of Co_3O_4 NPs for the fresh sample can possibly be a result of some oxidation during sample deposition.

It needs to be highlighted here that the aforementioned syntheses were carried out in aqueous solutions containing O_2. In order to investigate the role of dissolved O_2 on CoO_x NP formation during LASIS, control experiments were carried out in O_2 free DI-water by purging N_2 throughout the experiment. The results, as seen from dark field images of scanning mode TEM (STEM) in Fig. 4 (a), exhibit the formation of much larger hexagonal sheets (50-400 nm in diameter) that are confirmed to be single crystal β-$Co(OH)_2$ (JCPDS #30-0443) NPs from SAED and HRTEM analyses, as indicated in Fig. 4 (b) and (c). Again, the presence of a small amount of Co_3O_4 NPs in these images is suspected to arise due to oxidation during TEM sample preparations. The formation of this metastable β-$Co(OH)_2$ intermediate is primarily ascribed to the lack of O_2 in water that promotes the reaction pathway between ablated Co^{2+} ions and OH^- from water. However, after aging for three days, all the metastable β-$Co(OH)_2$ single crystals get fully oxidized into stable Co_3O_4 NPs in the colloidal solution, as indicated by the SAED patterns in Fig. 4 (d).

The chemical pathways, depicted schematically in Fig. 5, for the products evolution during LASIS on Co is believed to initiate the formation of two metastable reaction intermediates, i.e., CoO and β-$Co(OH)_2$, in the presence and absence of dissolved O_2 in the aqueous solution respectively. The formation of the intermediate Co^{2+} oxidation state can be ascribed to the ultrafast quenching rate due to the extreme temperature differences between plasma plume and liquid environment that initiates the partially oxidized and metastable crystallization states. Consequently, both intermediates transform to the final product of Co_3O_4 NPs through direct oxidation

and/or thermal decomposition during the ageing process in aqueous solutions even at standard ambient conditions. The chemical pathways discussed above also apply to the 1064 nm laser, as shown in the supporting information (Fig. S8).

B. Effect of laser parameters during LASIS on Co

A detailed investigation on the evolution of final products during LASIS on Co is presented for two laser wavelengths (1064 nm and 532 nm) and diffferent laser fluences through TEM images and PSD data in Figs. 6 & 7. The results presented here are for the final products of Co_3O_4 NPs after the ageing process. It is observed that ablation with 1064 nm laser at low fluence (0.9 J/cm^2) produces sparsely distributed NPs that have smaller sizes but irregular shapes. Corresponding particle size distribution (PSD) data from SMPS measurements on the aerosolized colloidal suspensions of NPs indicate a bimodal distribution with the dominant peak at ~8 nm and a secondary minor peak at ~30 nm, as seen from Fig. 6 (d). The observed size and morphology characteristics are indicative of vaporization and normal boiling as the dominant ablation mechanism, as explained later. In contrast, higher fluence (41 and 107 J/cm^2) ablation generates large concentration of agglomerates (Figs. 6 (b) & (c)) that comprises of spherical NPs with mono-modal size distribution (median size ~12 and 14 nm respectively). The respective PSDs in Figs. 6 (e) & (f) corroborate these observations by indicating the bimodal peaks being replaced by mono-modal peaks.

LASIS with 532 nm laser exhibit similar trends in NP morphology as observed for 1064 nm laser (TEM images in Figs. 7 (a)–(c)) except that the low laser fluence ablation generates dendritic NPs, as shown by Fig. 7 (a). The formation of dendritic NPs can probably be explained by the higher absorbance of 532 nm laser as compared to that of 1064 nm laser which promote extensive re-ablation and restructuring leading to neck formations among the already formed colloidal CoO_x NPs in the solution. The higher absorbance level of 532 nm is also indicated by UV-Vis spectroscopy data in the supporting documents and will be discussed later. Furthermore, the corresponding PSD data for 532 nm indicates a familiar shift, as observed in earlier 1064 nm case studies, from bimodal to mono-modal distribution

upon transitioning from low (1 J/cm^2) to high (43 and 114 J/cm^2) laser fluence cases respectively, as seen from Figs. 7 (d)-(f). The only observable difference in this case is that the NPs produced by 532 nm LASIS exhibits a higher average particle size (~13–22 nm) than the ones synthesized with 1064 nm laser (~10–14 nm). A possible explanation for the larger average particle sizes in this case is the coalescence and restructuring resulting from the re-ablation of already formed colloidal NPs by the highly absorptive 532 nm laser.

The aforementioned results are believed to be mainly consequences of the different ablation mechanisms. The commonly observed shifts in the PSDs from bi-modal to mono-modal peaks for low to high laser fluences, as reported above for 532 and 1064 nm LASIS cases, is possibly related to the onset of the more efficient explosive boiling as the ablation mechanism at higher laser energy. To be more specific, it is observed that during low fluence ablation, small bubbles form on the surface of the Co target, but the ablation process does not affect the bulk of the water body. This indicates vaporization and normal boiling as the two dominant ablation mechanisms under low laser fluence, wherein the nucleation of NPs are partly initiated by electron-phonon coupling within the plasma plume. This process largely produces charged NPs that do not undergo much aggregation and growth due to electrostatic repulsion.[2] At higher laser fluence, the dominant and more efficient explosive boiling generate much higher thermal energy in the plasma plume, as also physically observed by the drastic splashing of water around the laser beam accompanied by audible percussions. We believe that such high energy processes promote aggregation and coalescence that result in the mono-modal distribution of the primary NPs, as indicated earlier in Figs. 6 & 7.

Furthermore, calculated NP productivity per unit ablation area from ICP-OES measurement on NPs synthesized from LASIS using 1064 nm and 532 nm lasers, are compared in Fig. 8 (a). The NP generation increases with laser fluence up to a critical value of ~ 20-40 J/cm^2, beyond which the productivity of NPs starts to decrease for both 1064 nm and 532 nm lasers. The initial increase at low laser fluence is due to the transfer in ablation mechanism from vaporization and normal boiling to the more

effective explosive boiling. However, any further increase of the laser fluence induces secondary plasma at the liquid air interface which self-absorbs much of the laser power, thereby weakening the amount of energy that finally reaches the metal target.[5] In order to confirm this phenomenon, focused laser energy reaching the target after penetrating through an equivalent column of water was measured using a power meter. The results, as seen from Fig. 8 (b), reveal that the laser energy reaching the target surface indeed starts diminishing beyond a laser fluence of ~30 J/cm^2, which corresponds to the laser fluence of peak productivity in Fig. 8 (a). However, the percentage of penetrated energy over the original laser energy starts decreasing at even lower fluence (~15-20 J/cm^2). These measurements clearly support the explanation for the onset of self-absorption of laser energy by secondary plasma at liquid-air interface beyond the laser fluence of ~15-20 J/cm^2.

In relation to productivity, Fig. 8 (a) also indicates that at any laser fluence, 532 nm laser promotes a relatively higher ablation efficiency than 1064 nm laser. This is in agreement with previous studies indicating that LASIS with smaller wavelength lasers have a greater ability to ablate metal sub-surfaces, thereby providing higher ablation efficiency.[2] Here, it needs to be noted that the results are only for the first 15 minutes of ablation. For a detailed investigation on the effects of laser wavelengths on the ablation efficiency, NP concentrations are measured over longer periods of ablation time. The results, as shown in Fig. 8 (c), clearly demonstrate that the 532 nm laser produces higher NP concentration and larger ablation efficiency than 1064 nm laser during the first hour, which is in accordance with Fig. 8 (a). However, while LASIS with 1064 nm laser exhibits a continuous linear increase in NP concentration in time, LASIS with 532 nm laser indicates an increase in NP concentration up till an upper limiting value of ~80 mg/l, beyond which it plateaus off. Hence, continued ablation for two hours led to a distinctly higher concentration of NPs produced by 1064 nm laser as compared to those produced by the 532 nm laser. These results also corroborate our earlier theory that the high absorption of 532 nm laser by the suspended Co_3O_4 NPs in solution can significantly retard the ablation process.

A detailed investigation of the physics behind the aforementioned observations is

presented in Fig. 8 (d), indicating a comparison for the percentage of unfocused laser energy that penetrates through the colloidal suspension of CoO_x NPs in solution as well as an equivalent amount of DI-water for both 1064 nm and 532 nm lasers. The results indicate that for 1064 nm laser, ~65% of the original beam energy penetrates through the DI-water, as compared to ~85% of the beam energy that penetrates for 532 nm laser. The greater energy penetration (%) for 532 nm laser in water is mainly due to its higher photon energy, while a large amount of the 1064 nm laser energy is lost in thermal heating of the water. In contrast, for laser beams passing through colloidal solutions, the laser energy penetration (%) for 1064 nm laser barely changes as compared to only 30-40% of the 532 nm laser energy that reaches the target through the colloidal solution. These observations further demonstrate the higher absorbance of 532 nm laser by the colloidal NPs than that for 1064 nm laser. Such phenomenon can be attributed to the higher photon energy in 532 nm laser that is able to overcome the band gap barrier for electronic excitations in the colloidal NPs thereby accounting for the absorbance energy loss.

The mechanistic picture behind the effect of the re-ablation process due to the enhanced absorbance of 532 nm laser by colloidal NP suspensions is revealed through a series of re-ablation experiments conducted using 1064 nm and 532 nm lasers on identical NP solution samples. The results as shown by TEM images in Figs. 9 (a)-(c), compares the TEM image of an original LASIS generated NP sample in Fig. 9 (a) with TEM images of the same sample after 15 min of re-ablation using 1064 nm and 532 nm lasers, as seen from Figs. 9 (b) and (c) respectively. The TEM images along with the corresponding size distributions in Figs. 9 (d)-(f) collected from SMPS measurements, indicate that re-ablation by 532 nm laser generates spherical NPs with increased sizes (see Figs. 9 (c) & (f)). In contrast, colloidal NPs re-ablated by 1064 nm laser exhibit similar shape (Fig. 9 (b)) and size distributions (Fig. 9 (e)) as the ones in the original sample (Figs. 9 (a) & (d)). These observations are in accordance with our average size comparison results (Table S1 in supplementary data), and agree well with our earlier hypothesis that re-ablation by the more absorptive 532 nm laser can restructure and coalesce the colloidal NPs into uniform spherical shapes, thereby

increasing the peak NP sizes while weakening the primary ablation at the target surface. Such processes lower the overall productivity of NPs, but promote the restructuring of solution phase NPs into more uniform size and shapes.

C. Effect of solution-phase pH during LASIS on Co

In this final section, the effect of solution phase protonation on the ablation mechanism is studied by carrying out LASIS on Co target at different pH values of pH=7, pH=13 and pH=14 respectively. TEM images in Fig. 10 indicate that unlike the regular dendritic Co_3O_4 NPs formed at pH=7 (Fig. 10 (a)), the alkaline condition of pH=13 produces a large amount of Co_3O_4 nanorods (NRs) with average diameter of ~5 nm and length of ~100-200 nm (Fig. 10 (b)). Upon increasing the alkalinity to pH=14, the average diameter of the NRs increases to ~15 nm while keeping the similar length (Fig. 10 (c)). The corresponding HRTEM images and SAED patterns, as shown in Figs. 10 (d) & (e), demonstrate that both the NR structures at pH = 13 and 14 are composed of pure Co_3O_4, with (111) surface (d=0.466 nm) exposed to the surface. Our proposed chemical pathway for Co_3O_4 formation is depicted as following: first of all, both β-$Co(OH)_2$ and Co_3O_4 are more stable and prone to be formed in alkaline condition due to the reduced redox potential (see the Pourbaix-diagram of Co in Fig. S5). Secondly, the low solubility of $Co(OH)_2$ in alkaline condition promotes the thermal decomposition of the insoluble $Co(OH)_2$ into Co_3O_4 under LASIS conditions. The presence of β-$Co(OH)_2$ crystals is shown in Figs. 10 (b) & (c), as also confirmed by HRTEM images and SAED patterns for the crystal lattices (refer to Fig. S4 in supporting documents). Finally, the presence of large alkali metal K^+ ions in solution induces electrostatic interactions with closely-packed (111) lattice planes of Co_3O_4, that promotes the growth of β-Co_3O_4 NRs along the selective direction of the (111) plane.[48] Since decrease of redox potentials and presence of K+ ions are both facilitated by the solution-phase alkaline conditions, the growth of Co_3O_4 nanorods is predicted to be induced in the free liquid outside the laser induced cavitation bubble. The optical properties of the NP/NR samples produced under different pH conditions are revealed by the UV-Vis absorption spectra shown in Fig. 10 (f). Here, we have

confirmed through ICP-OES measurements that all three samples measured contain the same Co concentrations. The results indicate that the overall absorbance for all the NP/NR samples is enhanced as pH increases from 7 to14, which is partially due to the relative stability of Co_3O_4 NPs under alkaline conditions. However, the dramatic improvement in the absorption peak at ~410 nm (~3 eV), specifically for pH=13 sample, can be ascribed to the intensified LSPR that is strongly affected by sizes and shapes of nanostructured materials.[49] It is well-known that critical values for NP sizes dictate the enhancement or dampening of LSPR. Specifically, the LSPR peak for NRs is strongly impacted by the length-to-diameter-ratio (LTDR).[49] In this regard, the specific size and LTDR (~20-40) for the NRs (diameter of ~5 nm and length of ~100-200 nm) formed at pH=13 promotes the LSPR peak at 410 nm, as compared to the absence of the similar peak for the ones formed at pH=14 with an average diameter of 15 nm, as seen in Fig. 10 (e). Instead, the absorbance for the NRs at pH=14 case exhibits an overall higher absorbance at longer wavelengths of ~500–700 nm, which can be possibly attributed to its much smaller LTDR (~7-13). It needs to be pointed out here that the Co_3O_4 NRs are observed to form only at low laser fluence (<5 mJ/cm^2) cases in alkaline conditions. High fluence LASIS or RA completely reshapes them into spherical NPs (see Fig. S6). These observations further support the formation of the NRs as a result of ripening processes in the free liquid at an optimal temperature after the collapse of the cavitation bubble, since the solution-phase high temperatures induced by the otherwise high laser fluence conditions make them thermally unstable. Besides, we have also investigated LASIS on Co at other pH values, i.e., pH=2, 3, 10, and 12. However, our TEM results for LASIS products under low pH conditions (pH=2, 3) indicate similar morphologies for the NPs as obtained under pH=7 conditions, with the exception that the productivity is dramatically reduced due to the instability of metal oxides/hydroxides in acidic conditions. The pH=10 sample also shows similar NP morphology. On the other hand, sparse distribution of nanorods (NRs) are seen in the products under pH=12 conditions, thereby indicating that pH=12 is the threshold for NR formation. Our on-going investigations are focused on understanding and tuning the chemical physics behind

the formation of the NRs, in order to tailor their structure-property relations for their applications as water splitting catalysts or as doping materials for enhanced light absorption in photocatalysts.

Conclusion

In this article, we have presented a facile route for tailored synthesis of nanostructured oxides/hydroxides of Co using an in-house designed laser ablation synthesis in solution (LASIS) set-up that can be tuned for various experimental parameters. Specifically, we investigate the effects of laser parameters (wavelength, laser fluence) and solution phase properties (O_2 content, pH) on the size, shape, structure and composition of the resultant nanostructured materials produced from LASIS on bulk Co targets in aqueous solutions. Our results indicate that the chemical pathway during LASIS on Co in water leads to the formation of metastable intermediates such as CoO and single crystal β-$Co(OH)_2$ NPs in the presence and absence of solution-phase O_2 respectively. Both intermediates transform into Co_3O_4 NPs as the final products through oxidation and/or thermal decomposition in solution phase. In addition, we establish the role of the physics behind the different ablation mechanisms in tailoring the size and morphology of the final Co_3O_4 NPs. For both 1064 and 532 nm lasers, vaporization and normal boiling mechanism during LASIS at low laser fluence (<20 mJ/cm^2) dictates the formation of sparsely agglomerated NPs of bimodal size distribution. In contrast, the more efficient and explosive boiling presides as the dominant mechanism over the former two during LASIS at higher laser fluences that results in mono-modal size distributions of spherical shaped primary NPs in the agglomerates formed. Furthermore, we demonstrate that the high absorbance of 532 nm laser by solution-phase colloidal NPs promotes their re-ablation into spherical structures with increased average sizes. This is evident from the higher mean particle sizes (~13–22 nm) for NPs produced by 532 nm LASIS as compared to the ones synthesized with 1064 nm LASIS (~10–14 nm). To this end, we conclude that although the 532 nm laser indicates higher energy penetration through

the aqueous solutions, its self-absorption by colloidal NPs renders it less productive than ablation with 1064 nm laser over extended period of time. Finally, LASIS on Co in alkaline aqueous solutions (pH≥13) and low laser fluence conditions (<5 mJ/cm^2) produce Co_3O_4 nanorods (NRs) that exhibit enhanced LSPR properties in the visible range of ~400-410 nm wavelength. The aforementioned understanding of the chemical physics of laser ablation for different laser and solution phase parameters is fundamental to our critical design of LASIS for tailored synthesis of a wide variety metal/metal oxide nanostructured materials in future. In turn, the ability to synthesize such tailored complex nanostructures with unique optical properties via a facile, "green" synthesis route, as presented here, is promising for tuning their structure-property relations for applications such as photocatalysis and doping materials in nanocomposites with enhanced light absorption properties.

Acknowledgement: We acknowledge the financial support and funding for Sheng Hu (graduate student) through Sustainable Energy Education and Research Center (SEERC), UTK and financial support for Chad Meltone (undergraduate student) from Center for Materials Processing (CMP), UTK. We also thank Prof John Dunlap for all the technical help with TEM measurements.

References:

1. Barcikowski, S. & Compagnini, G. Advanced nanoparticle generation and excitation by lasers in liquids. *Phys. Chem. Chem. Phys.* **15,** 3022–6 (2013).

2. Amendola, V. & Meneghetti, M. What controls the composition and the structure of nanomaterials generated by laser ablation in liquid solution? *Phys. Chem. Chem. Phys.* **15,** 3027–46 (2013).

3. Blakemore, J. D., Gray, H. B., Winkler, J. R. & Mu, A. M. Co 3 O 4 Nanoparticle Water-Oxidation Catalysts Made by Pulsed-Laser Ablation in Liquids. *ACS Catal.* **3,** 2497–2500 (2013).

4. Amans, D. *et al.* Synthesis of Oxide Nanoparticles by Pulsed Laser Ablation in Liquids Containing a Complexing Molecule: Impact on Size Distributions and Prepared Phases. *J. Phys. Chem. C* **115,** 5131–5139 (2011).

5. Cristoforetti, G., Pitzalis, E., Spiniello, R., Ishak, R. & Muniz-Miranda, M. Production of Palladium Nanoparticles by Pulsed Laser Ablation in Water and Their Characterization. *J. Phys. Chem. C* **115,** 5073–5083 (2011).

6. Wang, C. X., Liu, P., Cui, H. & Yang, G. W. Nucleation and growth kinetics of nanocrystals formed upon pulsed-laser ablation in liquid. *Appl. Phys. Lett.* **87,** 201913 (2005).

7. Tsuji, T., Hamagami, T., Kawamura, T., Yamaki, J. & Tsuji, M. Laser ablation of cobalt and cobalt oxides in liquids: influence of solvent on composition of prepared nanoparticles. *Appl. Surf. Sci.* **243,** 214–219 (2005).

8. Amendola, V. & Meneghetti, M. Laser ablation synthesis in solution and size manipulation of noble metal nanoparticles. *Phys. Chem. Chem. Phys.* **11,** 3805–21 (2009).

9. Yan, Z., Bao, R., Huang, Y. & Chrisey, D. B. Hollow Particles Formed on Laser-Induced Bubbles by Excimer Laser Ablation of Al in Liquid. *J. Phys. Chem. C* **114,** 11370–11374 (2010).

10. Itina, T. E. On Nanoparticle Formation by Laser Ablation in Liquids. *J. Phys. Chem. C* **115,** 5044–5048 (2011).

11. Amendola, V., Riello, P. & Meneghetti, M. Magnetic Nanoparticles of Iron Carbide, Iron Oxide, Iron@Iron Oxide, and Metal Iron Synthesized by Laser Ablation in Organic Solvents. *J. Phys. Chem. C* **115,** 5140–5146 (2011).

12. Kevin Hagedorn, Bing Liu, and A. M. 2013IntermtallicPtPb_NP_LASIS_JElectrochemSoc_Hagedorn-F106-10.pdf. *J. Electrochem. Soc.* **160,** F106–F110 (2013).

13. Hur, T.-B., Phuoc, T. X. & Chyu, M. K. Synthesis of Mg-Al and Zn-Al-layered double hydroxide nanocrystals using laser ablation in water. *Opt. Lasers Eng.* **47,** 695–700 (2009).

14. Jiménez, E., Abderrafi, K., Abargues, R., Valdés, J. L. & Martínez-Pastor, J. P. Laser-ablation-induced synthesis of SiO2-capped noble metal nanoparticles in a single step. *Langmuir* **26,** 7458–63 (2010).

15. Zeng, H. *et al.* Violet photoluminescence from shell layer of Zn/ZnO core-shell nanoparticles induced by laser ablation. *Appl. Phys. Lett.* **88,** 171910 (2006).

16. Niu, K. Y. Hollow Nanoparticles of Metal Oxides and Sulfides Fast Preparation via.pdf. *Langmuir* **26,** 16652–16657 (2010).

17. Bai, G. *et al.* Porous Co3O4 nanowires and nanorods: Highly active catalysts for the combustion of toluene. *Appl. Catal. A Gen.* **450,** 42–49 (2013).

18. Liu, P. *et al.* Room temperature synthesized rutile TiO(2) nanoparticles induced by laser ablation in liquid and their photocatalytic activity. *Nanotechnology* **20,** 285707 (2009).

19. Liao, L. *et al.* Efficient solar water-splitting using a nanocrystalline CoO photocatalyst. *Nat. Nanotechnol.* 1–5 (2013). doi:10.1038/nnano.2013.272

20. Miotello, A. & Kelly, R. Laser-induced phase explosion : new physical problems when a condensed phase approaches the thermodynamic critical temperature. *Appl. Phys. A Mater. Sci. Process.* **73,** 67–73 (1999).

21. Park, K., Lee, D., Rai, a, Mukherjee, D. & Zachariah, M. R. Size-resolved kinetic measurements of aluminum nanoparticle oxidation with single particle mass spectrometry. *J. Phys. Chem. B* **109,** 7290–9 (2005).

22. Wagener, P., Ibrahimkutty, S., Menzel, A., Plech, A. & Barcikowski, S. Dynamics of silver nanoparticle formation and agglomeration inside the cavitation bubble after pulsed laser ablation in liquid. *Phys. Chem. Chem. Phys.* **15,** 3068–74 (2013).

23. Mortazavi, S. Z., Parvin, P., Reyhani, A., Golikand, A. N. & Mirershadi, S. Effect of Laser Wavelength at IR (1064 nm) and UV (193 nm) on the Structural Formation of Palladium Nanoparticles in Deionized Water. *J. Phys. Chem. C* **115,** 5049–5057 (2011).

24. Intartaglia, R. *et al.* Optical Properties of Femtosecond Laser-Synthesized Silicon Nanoparticles in Deionized Water. *J. Phys. Chem. C* **115,** 5102–5107 (2011).

25. Alrehaily, L. M., Joseph, J. M., Biesinger, M. C., Guzonas, D. a & Wren, J. C. Gamma-radiolysis-assisted cobalt oxide nanoparticle formation. *Phys. Chem. Chem. Phys.* **15,** 1014–24 (2013).

26. Compagnini, G. *et al.* Monitoring the formation of inorganic fullerene-like MoS2 nanostructures by laser ablation in liquid environments. *Appl. Surf. Sci.* **258,** 5672–5676 (2012).

27. Blandin, P. *et al.* Femtosecond laser fragmentation from water-dispersed microcolloids: toward fast controllable growth of ultrapure Si-based nanomaterials for biological applications. *J. Mater. Chem. B* **1,** 2489 (2013).

28. Singh, S. C. Effect of oxygen injection on the size and compositional evolution of ZnO/Zn(OH)2 nanocomposite synthesized by pulsed laser ablation in distilled water. *J. Nanoparticle Res.* **13,** 4143–4152 (2011).

29. Liu, X. *et al.* Co3O4/C nanocapsules with onion-like carbon shells as anode material for lithium ion batteries. *Electrochim. Acta* **100,** 140–146 (2013).

30. Sa, Y. J., Kwon, K., Cheon, J. Y., Kleitz, F. & Joo, S. H. Ordered mesoporous Co3O4 spinels as stable, bifunctional, noble metal-free oxygen electrocatalysts. *J. Mater. Chem. A* **1,** 9992 (2013).

31. Wen, Z. *et al.* A facile fluorine-mediated hydrothermal route to controlled synthesis of rhombus-shaped Co3O4 nanorod arrays and their application in gas sensing. *J. Mater. Chem. A* **1,** 7511 (2013).

32. Vijayakumar, S., Ponnalagi, a. K., Nagamuthu, S. & Muralidharan, G. Microwave assisted synthesis of Co3O4 nanoparticles for high-performance supercapacitors. *Electrochim. Acta* **106,** 500–505 (2013).

33. Patil, D., Patil, P., Subramanian, V., Joy, P. a & Potdar, H. S. Highly sensitive and fast responding CO sensor based on Co3O4 nanorods. *Talanta* **81,** 37–43 (2010).

34. Zhang, M., de Respinis, M. & Frei, H. Time-resolved observations of water oxidation intermediates on a cobalt oxide nanoparticle catalyst. *Nat. Chem.* **6,** 362–7 (2014).

35. Risch, M. *et al.* Atomic structure of cobalt-oxide nanoparticles active in light-driven catalysis of water oxidation. *Int. J. Hydrogen Energy* **37,** 8878–8888 (2012).

36. Yuan, C. *et al.* Lysine-assisted hydrothermal synthesis of urchin-like ordered arrays of mesoporous Co(OH)2 nanowires and their application in electrochemical capacitors. *J. Mater. Chem.* **20,** 10809 (2010).

37. Sun, X. *et al.* Morphology controlled high performance supercapacitor behaviour of the Ni–Co binary hydroxide system. *J. Power Sources* **238,** 150–156 (2013).

38. Gong, L. & Su, L. Facile synthesis and capacitive performance of the Co(OH)2 nanostructure via a ball-milling method. *Appl. Surf. Sci.* **257,** 10201–10205 (2011).

39. Wang, Z., Chen, X., Zhang, M. & Qian, Y. Synthesis of Co3O4 nanorod bunches from a single precursor Co(CO3)0.35Cl0.20(OH)1.10. *Solid State Sci.* **7,** 13–15 (2005).

40. Zhu, H. T. *et al.* Synthesis and magnetic properties of antiferromagnetic Co3O4 nanoparticles. *Phys. B Condens. Matter* **403,** 3141–3145 (2008).

41. Thangavelu, K., Parameswari, K., Kuppusamy, K. & Haldorai, Y. A simple and facile method to synthesize Co3O4 nanoparticles from metal benzoate dihydrazinate complex as a precursor. *Mater. Lett.* **65,** 1482–1484 (2011).

42. Karthick, S. N., Hemalatha, K. V., Justin Raj, C., Kim, H. J. & Yi, M. Synthesis of nano-bound microsphere Co3O4 by simple polymer-assisted sol–gel technique. *J. Nanoparticle Res.* **15,** 1474 (2013).

43. Liu, Z., Ma, R., Osada, M., Takada, K. & Sasaki, T. Selective and controlled synthesis of alpha- and beta-cobalt hydroxides in highly developed hexagonal platelets. *J. Am. Chem. Soc.* **127,** 13869–74 (2005).

44. Yang, J., Liu, H., Martens, W. N. & Frost, R. L. Synthesis and Characterization of Cobalt Hydroxide, Cobalt Oxyhydroxide, and Cobalt Oxide Nanodiscs. *J. Phys. Chem. C* **114,** 111–119 (2010).

45. Zheng, L. *et al.* Capping agent free synthesis of PtSn bimetallic nanoparticles with enhanced electrocatalytic activity and lifetime over methanol oxidation. *Catal. Commun.* **9,** 624–629 (2008).

46. Armbrüster, M., Wowsnick, G., Friedrich, M., Heggen, M. & Cardoso-Gil, R. Synthesis and catalytic properties of nanoparticulate intermetallic Ga-Pd compounds. *J. Am. Chem. Soc.* **133,** 9112–8 (2011).

47. Gallant, D., Pézolet, M. & Simard, S. Optical and Physical Properties of Cobalt Oxide Films Electrogenerated in Bicarbonate Aqueous Media. *J. Phys. Chem. B* **110,** 6871–6880 (2006).

48. Ke, X. *et al.* Molten salt synthesis of single-crystal Co3O4 nanorods. *Mater. Lett.* **61,** 3901–3903 (2007).

49. Jiang, R., Li, B., Fang, C. & Wang, J. Metal/Semiconductor Hybrid Nanostructures for Plasmon-Enhanced Applications. *Adv. Mater.* n/a–n/a (2014). doi:10.1002/adma.201400203

Figures:

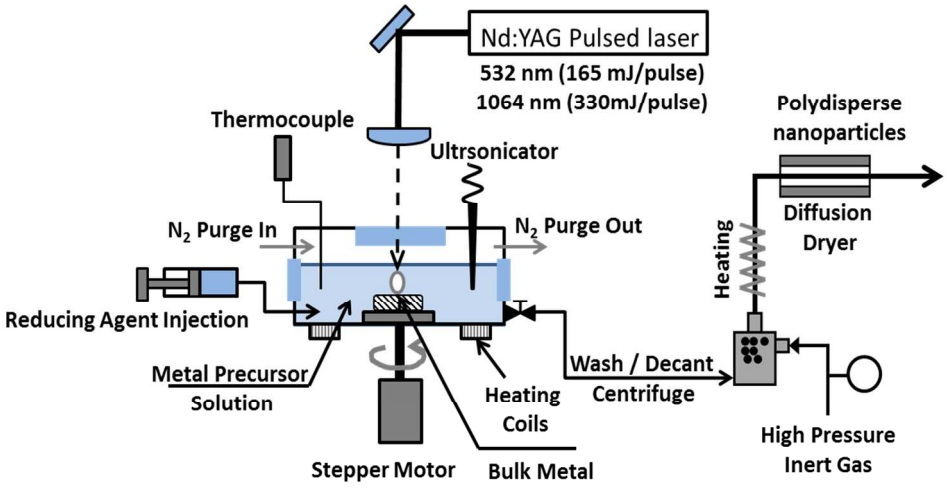

Fig. 1 Schematic diagram of the designed multi-functional LASIS setup

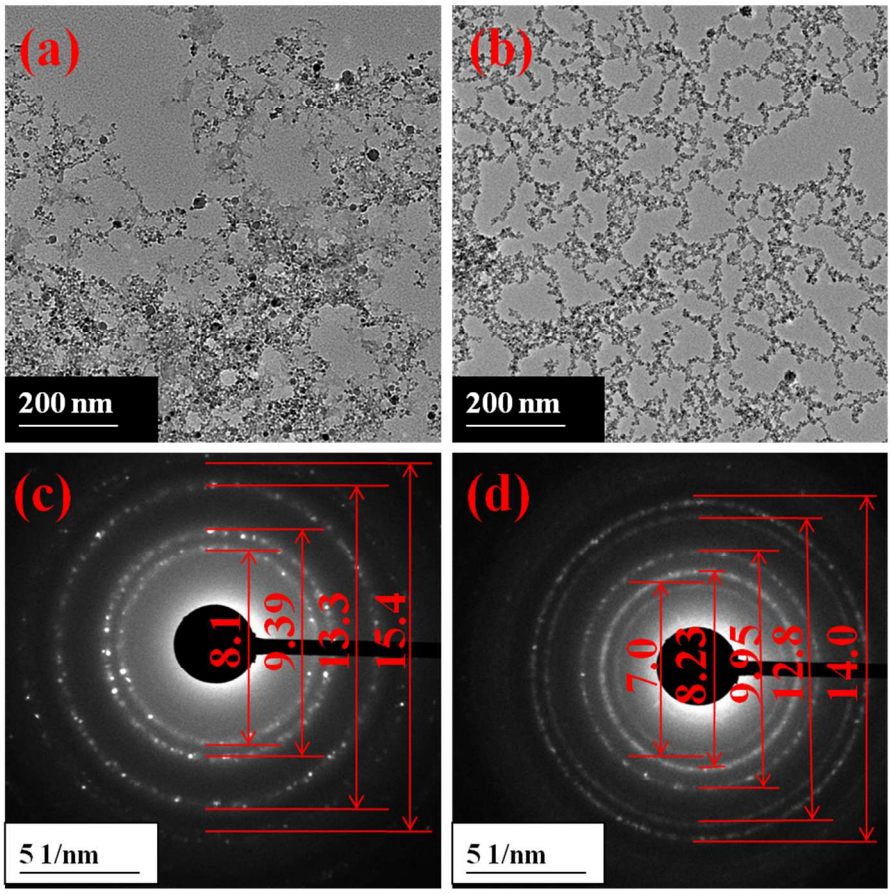

Fig. 2 TEM images **(top)** and the corresponding SAED patterns **(bottom)** showing evolution of CoO_x NPs from LASIS by 532 nm laser at 1 J/cm^2: **(a), (c)** fresh sample; **(b), (d)** aged for three days.

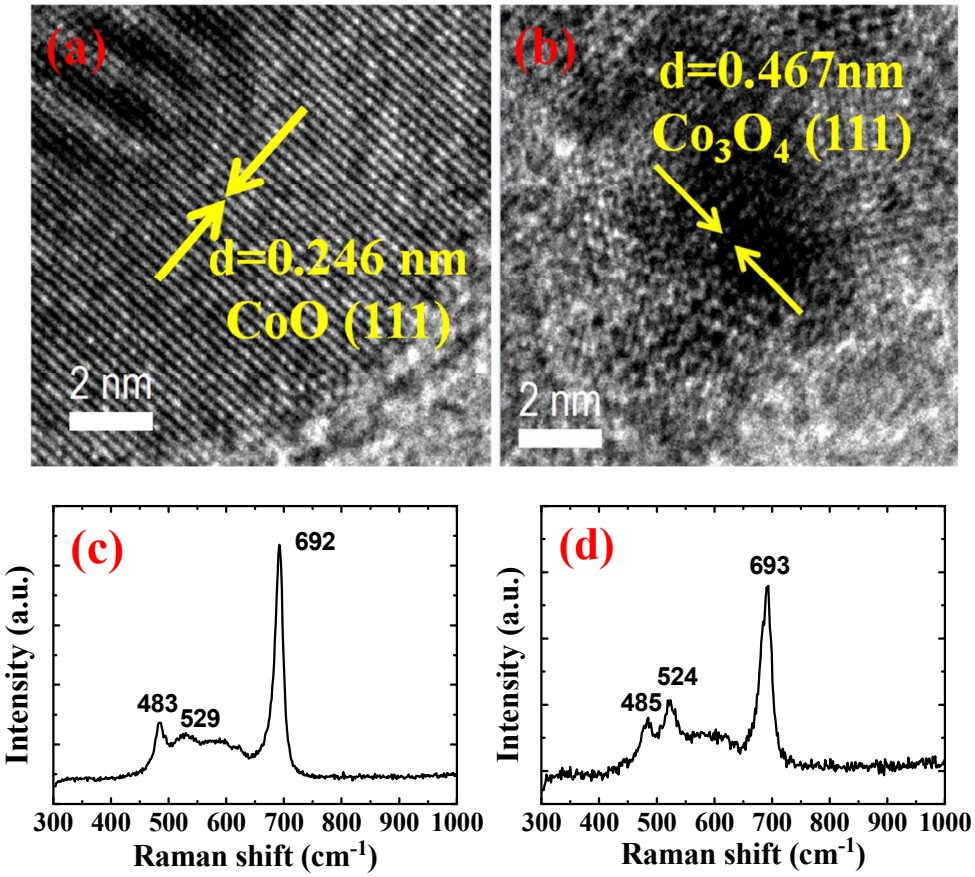

Fig. 3 (a), (b) HRTEM images, and **(c), (d)** Raman spectra for CoO_x NPs prepared by 532 nm laser at laser fluence of 1 J/cm^2; **(a), (c)** fresh sample; **(b), (d)** aged for three days.

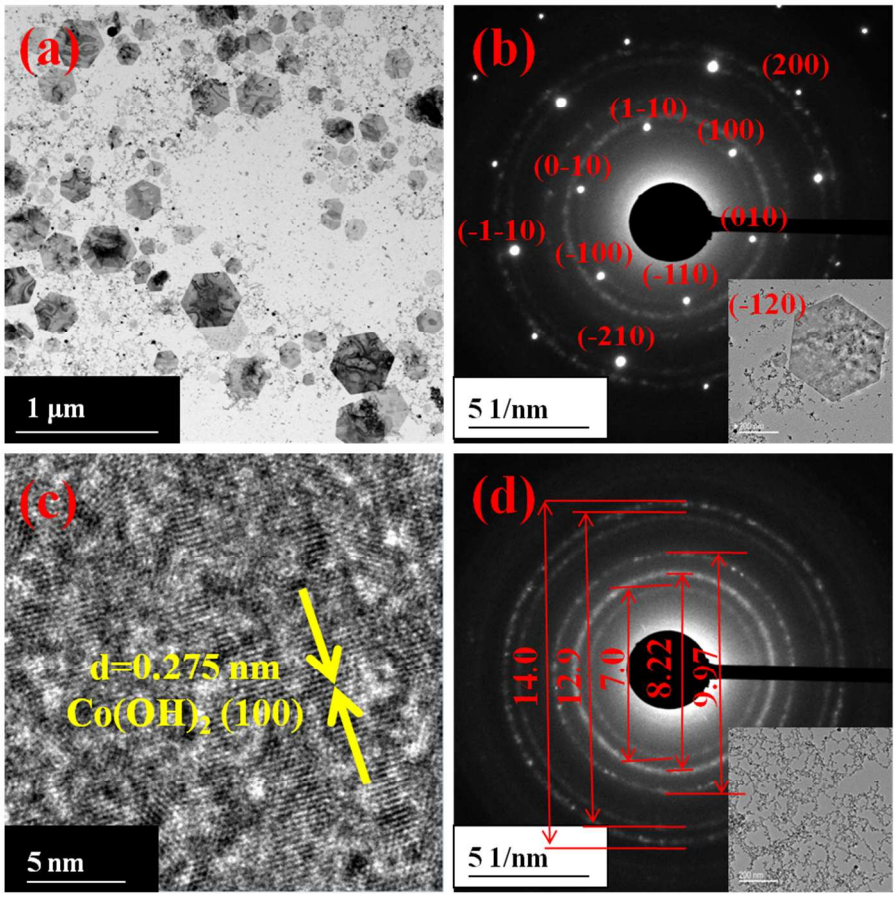

Fig. 4 (a), (b), (c): Freshly prepared NPs from LASIS by 532 nm laser (1 J/cm^2) with N_2 purge generates hexagonal β-$Co(OH)_2$ crystals along with Co_3O_4 NPs; **(a)** Bright field STEM image; **(b)** SAED pattern indicating single crystal β-$Co(OH)_2$ NP on <001> zone axis (Inset: corresponding TEM image); **(c)** HRTEM image for β-$Co(OH)_2$ crystal showing the lattice d-spacing; **(d)** SAED pattern of the sample aged for three days indicating Co_3O_4 NPs (Inset: corresponding TEM image, the scale bars are 200 nm).

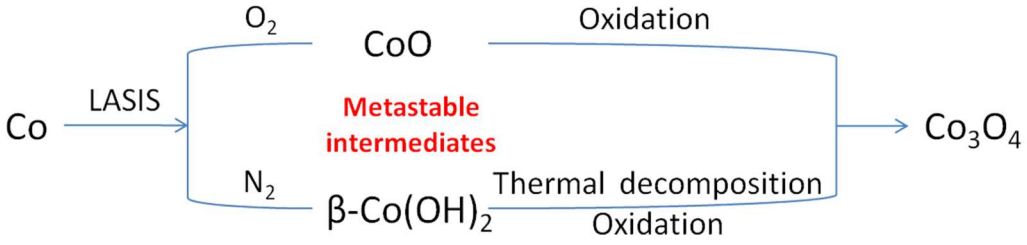

Fig. 5 Chemical pathway for the formation of Co_3O_4 NPs via LASIS on Co with/without dissolved O_2.

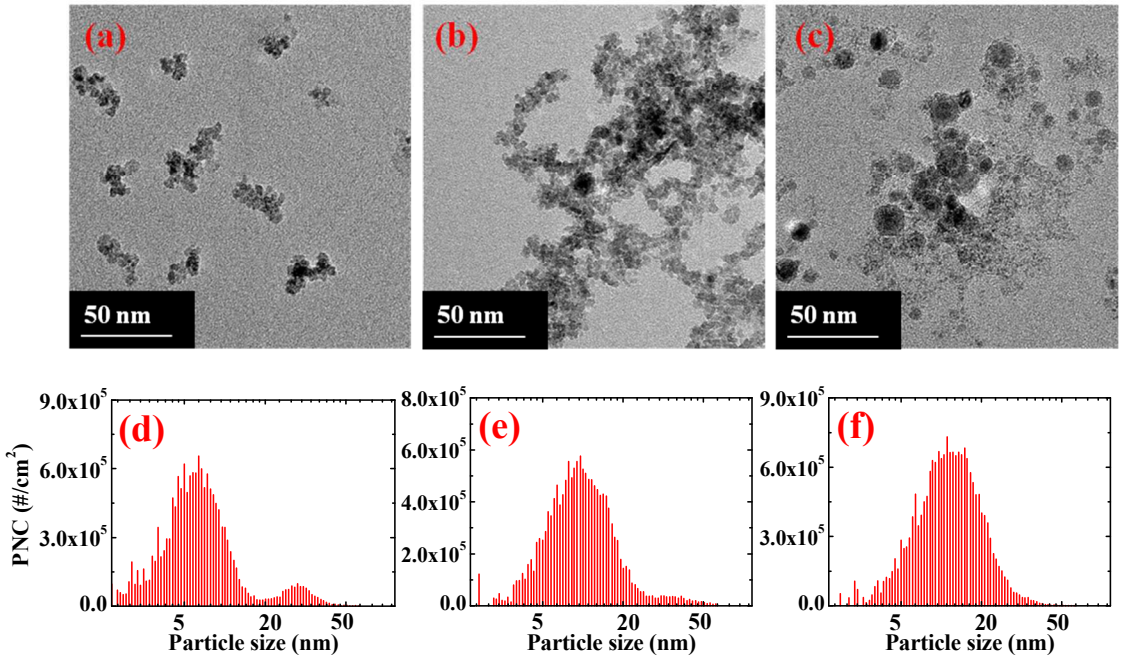

Fig. 6 TEM images **(top)** and particle size distributions (PSD) **(bottom)** for 1064 nm laser ablated Co_3O_4 NPs at different laser fluences: **(a), (d)** 0.9 J/cm^2; **(b), (e)** 41 J/cm^2; **(c), (f)** 107 J/cm^2. The vertical axis of PSD shows the particle number concentration (PNC).

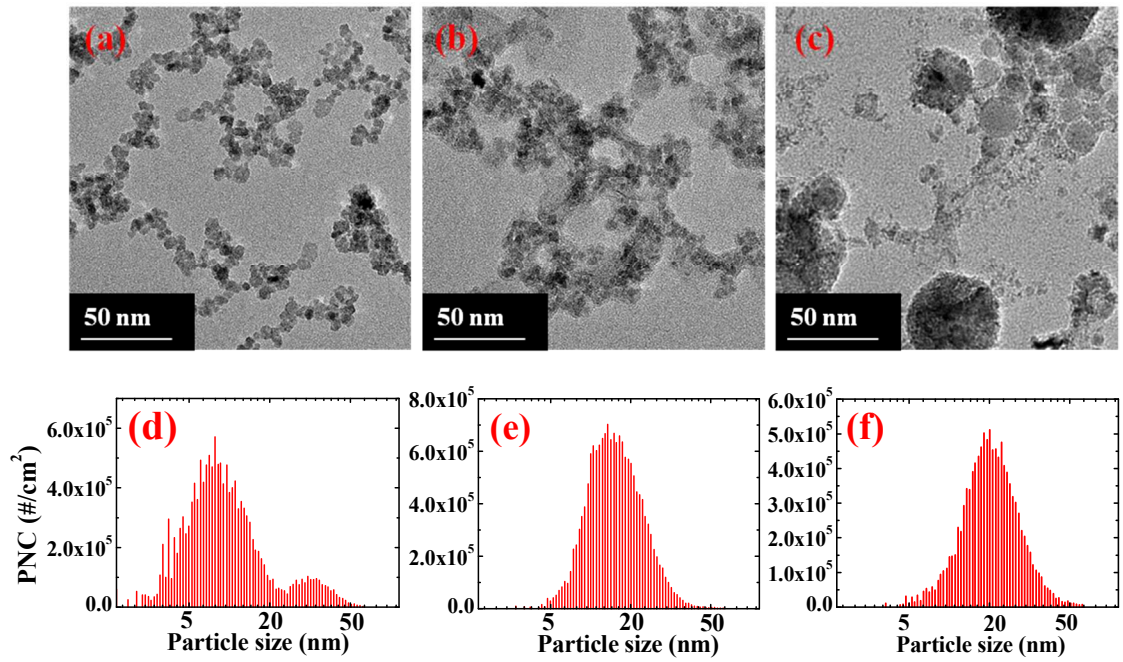

Fig. 7 TEM images **(top)** and particle size distributions (PSD) **(bottom)** for 532 nm laser ablated Co_3O_4 NPs at different laser fluences: **(a), (d)** 1.0 J/cm^2; **(b), (e)** 43 J/cm^2; **(c), (f)** 114 J/cm^2. The vertical axis of PSD shows the particle number concentration (PNC).

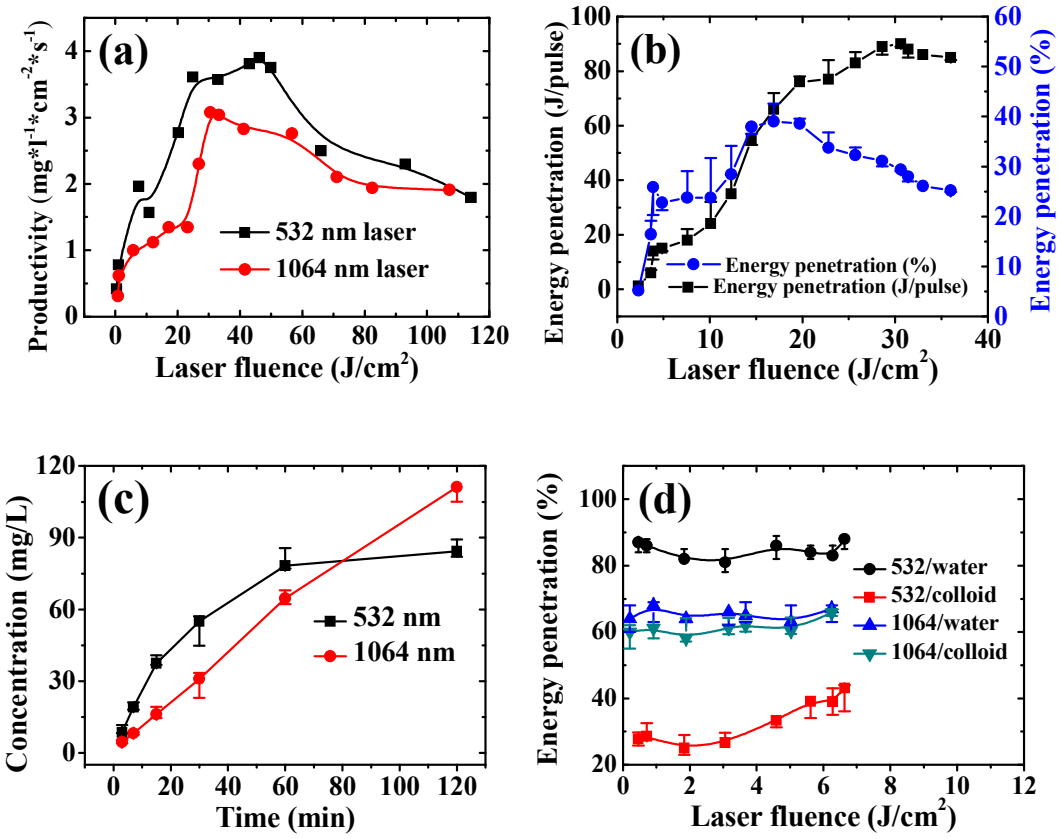

Fig. 8 (a) Specific area productivity of Co_3O_4 NPs per unit ablation time; **(b)** Focused laser energy (1064 nm) penetration (%) through a glass of DI-water at different laser fluences, where energy penetration (%) is the ratio of penetrated laser energy over the original laser energy; **(c)** NP concentration evolution in time for low laser fluence case of ~0.3 J/cm^2. **(d)** Unfocused laser energy (1064 nm and 532 nm) penetration (%), through Co_3O_4 colloid as well as an equivalent column of DI-water.

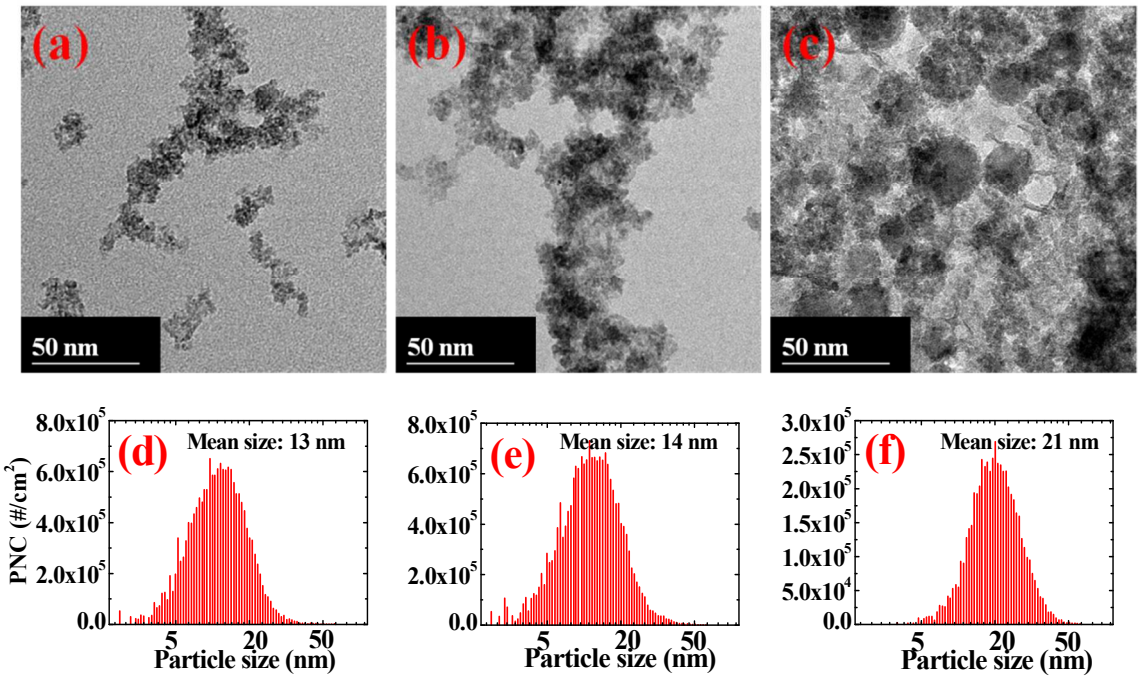

Fig. 9 TEM images showing: **(a)** the original NPs generated by LASIS and the alterations in their sizes and shapes after re-ablation (laser energy of 170 mJ/pulse) with: **(b)** 1064 nm laser and **(c)** 532 nm laser; **(d)-(f)** indicate PSDs corresponding to the samples shown in **(a)**, **(b)**, and **(c)** respectively.

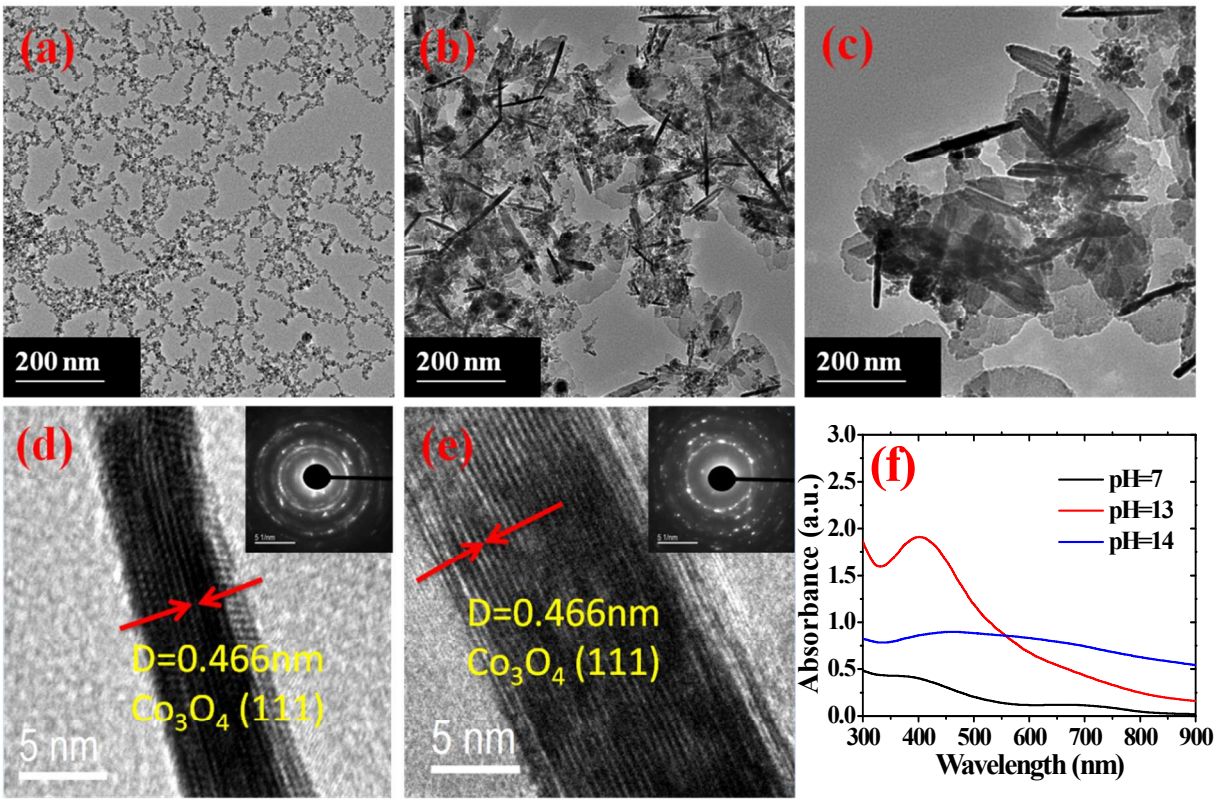

Fig. 10 (a)-(c) TEM images of Co_3O_4 NPs obtained from LASIS at: **(a)** pH=7; **(b)** pH=13; **(c)** pH=14; (532 nm laser at a fluence of ~1 J/cm^2); **(d), (e)** the corresponding HRTEM images for the case of: **(d)** pH=13 and **(e)** pH=14; (Insets: SAED patterns); **(f)** UV-Vis absorption spectra for colloidal NPs synthesized at different pH values.

Tables:

Table 1 Comparison of standard and experimental d-spacing calculated from SAED

Standard d-spacing (A)		**Experimental d-spacing (A)**	
CoO	Co_3O_4	Fresh sample	Aged for three days
	2.86 (220)		2.85
2.46 (111)	2.44 (311)	2.47	2.43
2.13 (200)	2.02 (400)	2.13	2.01
1.51 (220)	1.56 (333)	1.50	1.56
1.29 (311)	1.43 (440)	1.30	1.43